Nanoscale

Accepted Manuscript

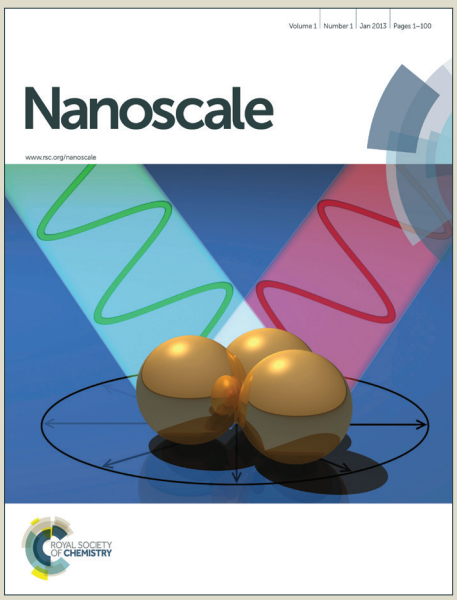

ROYAL SOCIETY OF CHEMISTRY

www.rsc.org/nanoscale

The oriented growth of tungsten oxide in ordered mesoporous carbon and their electrochemistry performance

Tao Wang,[a] Jing Tang,[b] Xiaoli Fan,[a] Jianhua Zhou,[c] Hairong Xue,[a] Hu Guo,[a] and Jianping He*[a]

Abstract: Electrocatalysts for hydrogen oxidation and methanol oxidation are the heart of proton exchange membrane fuel cell. In spite of tremendous efforts, developing low-cost anodic electrocatalysts with high catalytic activity and corrosion resistance is still a great challenge. Here, we report a nanocomposite consisting of WO_3 nanorod orientated grow in ordered mesoporous carbon as a high-performance functional catalyst carrier for proton exchange membrane fuel cell. As a result of the catalytic graphitization effect of tungsten compounds, the degree of graphitization and conductivity of mesoporous carbon film can be obviously improved even at a low temperature. Furthermore, compared to ordered mesoporous carbon, ordered mesoporous C-WO_3 nanocomposites possess favorable hydrophilicity, excellent corrosion resistance and distinguished electrocatalytic activities. The unusual electrocatalytic activities arise from the ideal physical properties of the carrier and synergetic catalysis between Pt and WO_3.

Keywords: ordered mesoporous material, orientated growth, catalytic graphitization, synergetic electrocatalysis

1. Introduction

Proton exchange membrane fuel cell (PEMFC) as an environmentally friendly energy conversion technology and a representative of the fourth generation of electricity generator, is

widely recognized as the new generation of power source to compete with internal combustion engine.[1-4] Catalyst which can accelerate the redox reactions on electrodes is one of the core parts in PEMFC. Although precious metal catalysts such as Pt, Pd, Ru and their alloys have been considered as the most efficient catalysts, researchers are still devoting to investigating other low- or non-precious metal catalysts based on the consideration of cost and sustainable development.[5,6] The possible low- or non- precious metal catalysts mainly include non-metal composites, transition metal oxides, sulfide, carbide and their hybrid with precious metal. For example, the recent nitrogen doped carbon composite is one of the well-known nonmetal catalyst which exhibit excellent catalytic activity for oxygen reduction reaction.[7] Tungsten trioxide (WO_3) is also known to be able to form a nonstoichiometric hydrogen tungsten bronze (H_xWO_3) compound in acid solution.[8] As reported by many researches, Pt-WO_3 catalyst supported on active carbon or Pt catalyst supported on pure WO_3 exhibit a much higher electrochemical activity due to the inherit electrocatalytic activity of WO_3 for redox reactions and the assistant catalytic effect between Pt and WO_3.[9,10]

In order to decrease the utilization amount of catalysts while retaining high electrochemical activity, catalysts are usually deposited on high surface area supports. In the past decade, mesoporous materials such as silica, metal oxides and carbon have attracted great interests due to their widely potential application in sensor, gas storage, drug transport, electrochemical energy storage and fuel cells.[11-18] Thereinto, ordered mesoporous carbon is a promising catalyst supports due to their rich sources, chemical and mechanical stability, high specific surfaces area and adjustable pore structures[19-23]. However, the electric conductivity and anticorrosion of carbon materials are not comparable to other non-carbon supports, which need further modification.[24,25]

More interesting, the regular structure of ordered mesoporous carbon can provide a confined space for the growth of low dimensional nanomaterials with adjustable morphology, structure, component and functionality, which could form a unique nanosystem that might exhibit a distinguished performance in PEMFC. Previously, ordered mesoporous nanomaterials such as silica were used as the template for the growth of low dimensional nanometals and nanometal oxides. Tolbert *et al.* prepared cobalt nanoparticle chains within the silica pores and obtained altered magnetic coupling due to the effect of nanoscale confinement.[26] Recently, Yamauchi *et al.* synthesized noble metal (Pt, Au and Ag) nanowires by taking advantage of the mesochannels in mesoporous silica (SBA-15). In addition, the length of the metal nanowires is easily controlled by the reduction time.[27] Similar to the nanometals, low dimensional metal oxides are also controlled developed within the confined space of ordered mesoporous materials.[28-30] Ordered mesoporous carbon prepared from low molecular weight carbon source has large surface area, adjustable pore size and confined channel space, which provide the possibility as the template for the growth of low dimensional nanomaterials. Zhao et al synthesized ordered mesoporous carbon with uniform metal-containing nanoparticles which are partially embedded in the carbon framework with the remaining part exposed in the mesopore channels.[31] The special semi-exposed structure provides a good confinement effect and exposed surface for catalysis, and helps to limit the nanoparticles and prevent aggregating during catalysis.

In this work, we first provide a novel method for controllable growth of low dimensional tungsten oxide nanodots, nanowires and nanorods within the frameworks of ordered mesoporous carbon. The tungsten oxide modified mesoporous carbon composites not only exhibit an improved graphitization degree and hydrophilic ability but also show an excellent electrochemical activity

and anticorrosion performance when they are used as Pt catalysts support in PEMFC.

2. Results and Discussion

2.1 Ordered mesoporous C-WO_3 film-effect of the tungsten compound content

In order to investigate the effect of tungsten compound content on the ordered mesoporous structure, graphitization degree, and corrosion resistance of the mesoporous carbon-based film, different amounts of tungsten source were added during the self-assembly process. As demonstrated by the energy dispersive X-ray spectrum (EDS) (Fig. S1a,b) of ordered mesoporous C-WO_3 film offered in the ñSupplementary contentò, tungsten has been successfully introduced into the framework of the amorphous ordered mesoporous carbon. There are peaks of Si appears in the Fig. S1 because of the small amount of silicon in silicotungstic acid. Further, we make a careful analysis of the state of W elements in ordered mesoporous films by XPS test, as shown in Fig. 1 and Fig. S1c. The thick black line is the original test data, the red thick line is the total fitting data, and the rest of color filaments are fitting data.

C_{1s} spectrums of CW-0%-500 and CW-10%-500 are presented in Fig. 1a. The C_{1s} spectrum of CW-0%-500 can be deconvoluted into five peaks, locating at 281.1, 281.6, 283.0, 284.2 and 288.5 eV, respectively. The binding energy of 281.1 and 281.6 eV are assigned to C-H or amorphous carbon,[32] the binding energy peak at 284.2 eV represents the pure graphitic sites,[33] another binding energy peak of 283.0 eV corresponds to the C-O or amorphous carbon atoms,[34] and the highest peak at 288.5 eV is mainly close to the C-O or C=O bond.[35,36] The C_{1s} spectrum of CW-10%-500 can be fitted into six peaks centered around 281.9, 282.4, 282.8, 283.5, 284.3 and 287.8 eV, respectively. The binding energy peaks at 281.9 and 282.8 eV can be attributed to C-O or amorphous carbon atoms,[32,34] the peak centered at 282.4 eV is assigned to SiC,[37] the peak at 283.5

eV corresponds to WC,[38] peak at 284.3 eV represents the pure graphitic site[33] and peak of 287.8 eV is associated with C=O.[39] Comparing the peak area between 281 and 282 eV (represent the amorphous carbon) with that of 284.3±0.2 eV (represent the graphitic carbon), we can find out that the graphitic carbon content in CW-10%-500 is higher than that in CW-0%-500, suggesting that the addition of tungsten accelerate the graphitization of amorphous carbon during carbonization.[40]

Fig. 1b presents the W_{4f} spectrum of obtained CW-10%-500, which can be deconvoluted into six peaks at 30.7, 31.5, 32.9, 33.3, 35.2 and 37.4 eV. The peaks at 30.7 and 31.5 eV are weak which represent the low content of metallic W[41] and WC,[42] respectively. The other intense peaks centered at 32.9, 33.3, 35.2 and 37.4 eV can be assigned to W^{4+}, W^{6+} and the transition state between W^{4+}~W^{6+} in W-O,[42] indicating that W mainly existed in the form of tungsten oxide and WO_3 owns the highest content. We infer that silicotungstic acid initially decompose into SiO_2 and WO_3 during the high temperature treatment, and then a part of WO_3 is in-situ reduced into other tungsten compound, such as WO_2, WC or W.

The small-angle XRD patterns of the mesoporous films are shown in Fig. 2a. An intense Bragg diffraction peak was observed at around $2d = 1°$, indicating an ordered mesoporous structure. The intensity of the peak became weak along with the increase of content of WO_3, suggesting that excessive WO_3 would induce a deterioration of the long-range structural order. The details will be discussed later in the section of TEM and growth mechanism of WO_3 analysis. Wide-angle XRD patterns of the mesoporous films are shown in Fig. 2b, which is helpful to analyze the crystalline state of tungsten compound and the graphitization degree of carbon. Due to a low content of carbon and high contents of hydrogen and oxygen in the calcined phenolic resin at temperatures of

350-600 °C, the frameworks of products resemble resin polymers.[43,44] In fact, the phenolic resin is very difficult to be graphitized even after being carbonized at 1000 °C.[43,45,46] Ordered mesoporous pure carbon film (CW-0%-500) only has a broad diffraction peak around 2ɗ of 19°, which is attributed to the amorphous carbon. With the increase of WO_3 content, the broad diffraction peak around 2ɗ of 19° shifts toward right and the (002) diffraction of carbon at 2ɗ of 26° gradually becomes more resolved, indicating that the graphitization degree of carbon framework is enhanced by the addition of tungsten compound. Furthermore, we can observe the peaks of tungsten compound in the wide-angle XRD patterns. The diffraction peaks at 2ɗ values of about 23.3, 29.7 and 32.8° are attributed to WO_3 (JCPDS card No. 20-1324), the very weak diffraction peaks at 31.5 and 35.6° are attributed to WC (JCPDS card No.25-1047). By contrasting the peak intensity of WO_3 and WC, we infer that the content of WO_3 is higher than that of WC, which is consistent with the XPS analysis. When the WO_3 content reaches 10% or more, the graphitization degree of carbon framework is further heighten. As a result, the peak around 26° is broader and higher, which may mask the peaks of tungsten compound. Normally, the characteristic WO_3 vibrations are at about 805, 715, and 270 cm^{-1} in Raman spectra (Fig. 3).[47-49] However, it is difficult to observe the tungsten oxide peaks in the Fig. 3(b-e) or Fig. 7. The samples (CW-x-500) still remain resin polymers because of the low calcination temperature (Ò500 °C), and result in a fluorescence interference in Raman spectra.[43,44] Besides, the contents of tungsten oxides are low. Therefore, we can observe a slant background in Fig. 3, donôt find the peaks of tungsten oxide. After being heated at or over 600 °C, the resin polymer framework would transfer into amorphous carbon, and the fluorescence interference disappear.[43,44] If we choose the part of Raman spectra of CW-10%-700 (Fig. S2), we can see two broad bands, which belong to the amorphous tungsten

oxide or low crystallinity tungsten oxide, which are agree with the wide-angle XRD (Fig. 2b) and the high resolutionï TEM image (Fig. 5e3). The first band (200-500 $cm^{ï 1}$), is associated to O-W-O bending modes; the second range (600-1000 $cm^{ï 1}$), is associated to W-O stretching modes.[48]

The graphitic structure of the obtained C-WO_3 films is further confirmed by Raman spectra (Fig. 3). The peak at around 1580 $cm^{ï 1}$ (*G* band) is associated with the E_{2g} vibrational mode of sp^2 hybridized carbon atoms (graphitic structure), the other peak at about 1350 $cm^{ï 1}$ (*D* band) is usually referred to as vibrations of sp^3-hybridized carbon atoms (turbostratic components). The relative intensity of the *D* and *G* lines (I_D/I_G) is usually used to demonstrate the graphitic degree of carbon materials.[50,51] It is obvious that the peaks of *D* and *G* both gradually strengthen along with the increases of W in carbon films, and the relative intensity of the *D* and *G* lines is also enhanced. Because of the low calcination temperature (Ò 500 °C), the samples (CW-x-500) still resemble resin polymers, which lead to a fluorescence interference in Raman spectra.[43,44] We have calculated the value of I_D/I_G by deducting fluorescence interference. As shown in Table 1 and Table S1, we find that the I_D/I_G values of the samples decrease along with the incorporation of tungsten compound, suggesting the enhanced graphitization degree of samples. The results indicate that the W species can accelerate the carbonization of resol and transformation of amorphous carbon to graphite.[40] Generally, there are two kind of catalytic graphitization mechanisms of carbon by various metal or metal compound: the carbon dissolution-precipitation mechanism and the carbide formation-decomposition mechanism.[52,53] According to the previous study, the scientists conclude that the catalysts retained as metal belong to the carbon dissolution-precipitation mechanism, such as Fe, Co, Ni, and those retained as carbide belong to the carbide formation-decomposition mechanism, such as Ti, Mo, W.[53] In the carbon

dissolution-precipitation mechanism, $yC_{(disordered)} + Me \rightarrow MeC_y \rightarrow Me + yC_{(Graphite)}$; in the carbide formation-decomposition mechanism, *metal oxide or metal + C → carbide → metal + easily graphitizable carbon → metal + graphite*.[54] In this study, it is reasonable to conclude that the amorphous carbon was partly catalytically graphitized by tungsten compound based on the carbide formation-decomposition mechanism.[53,55,56] Moreover, tungsten compound promoted the formation of turbostratic carbon in addition to the graphitic component (shown in Fig. 3), which is consistent with the results of literature.[53] We further conducted the electrical conductivity test of C-WO_3 films to infer the graphitic degree of carbon materials because electrical conductivity is proportional to the graphitization degree of carbon. According to electrical conductivity analysis (concluded in Table 1), CW-0%-500 possesses the lowest electron conductivity while the electron conductivity of C-WO_3 films increases along with the more addition of W species. It is probably due to the improved graphitic degree which results from the catalytic graphitization of amorphous carbon by W compound and the existence of WC and metallic W in C-WO_3 films. The static contact angle test was performed to characterize the surface hydrophilicity of films. Results are collected in Table 1 and the macroscopic low-magnification photomicrographs of the static contact angles for all films samples are illustrated in Fig. S3. The test data indicates that the ordered mesoporous C-WO_3 films are more hydrophilic than ordered mesoporous pure carbon film (CW-0%-500) due to the existence of hydrophilic WO_x. Thus, the static contact angles of C-WO_3 films decrease from 71° to 61° when the content of W increases from 0 to 20%. We infer that the C-WO_3 films with a lower water contact angle would be helpful for Pt loading and promote the electrocatalytic reaction because of the enlarged three-phase interface.

Fig. 4 illustrates the N_2 adsorption-desorption isotherms and corresponding pore size

distribution curves of ordered mesoporous C-WO_3 films. The structural parameters of the films, including the BET surface area (S_{BET}), average pore size (D), percentage of mesopores (R_{meso}) and total pore volume (V_{total}) are presented in Table 2. When the percentage content of WO_3 Ò 10%, the N_2 adsorption-desorption isotherms of these mesoporous C-WO_3 films after pyrolysis at 500 ℃ in nitrogen atmosphere (Fig. 4a) show a typical type IV curve with a H_1-type hysteresis loop and a distinct condensation step, indicating uniform columnar mesopores. Since the rigid WO_3 and SiO_2 exist, the heat shrinkage of ordered mesoporous carbon film framework decreased (Fig. 4b). Thus, compared with ordered mesoporous carbon (CW-0%-500), ordered mesoporous C-WO_3 films have higher BET surface area, larger average pore size and higher total pore volume. When the percentage content of WO_3 reaches to 20%, its structural parameter is poor, which suggests that the excessive addition of silicotungstic acid would destroy the ordered mesoporous structure of carbon film. In this case, excess silicotungstic acid would hydrolyze and then be formed into bulk, which perturbed the assembly of F127 and resol.

We observed the internal microscopic structure of carbon membrane with different tungsten content through TEM analysis and illustrated the images in Fig. 5. Pure carbon material (CW-0%-500) and carbon-tungsten oxides composites prepared in this paper, have a highly ordered hexagonal mesostructure, which presents typical stripe-like and hexagonally arranged images, viewed from the [110] and [001] directions, respectively.[43,57] Therefore, we can see that the TEM images of the Fig. 5c2 and part of Fig. 5b1 is viewed from the [001] direction, while the others is viewed from [110] direction. As shown in the TEM images of C-WO_3 films in Fig. 5b-e, lots of one-dimensional rods regularly disperse in ordered mesoporous carbon frameworks which gradually get longer and thicker along with the improved content of tungsten. They are mainly

ascribed to tungsten trioxide through the following mechanism discussion. As shown in Fig. 5b, when the tungsten content is 2.5% in the carbon composites, there are plenty of short needle-like particles with the diameter of 10 ± 2nm and length of 60 ± 20 nm embed in the carbon framework and parallel to the channels. When the tungsten content is up to 5%, the ñthin needlesò grow up to the rod-shaped stuff with the diameter of 60 ± 20 nm and the length of 150 ± 50 nm. After the tungsten content continuously increases to 10%, the ordering of the tungsten-carbon composites decreased due to the large amount of long rod-shaped stuff with a length of up to 600 nm. At this point, tungsten content is near saturation and we infer that excessive tungsten will surpass the limit of the confined effect of mesoporous carbon. As expected, the tungsten-carbon composites lose their ordering mesoporous structure due to the over-grown rod-shaped stuff which casually crosses the carbon framework. However, the density of tungsten compounds embedded in the CW-20%-500 is similar to that of CW-10%-500. The excessive tungsten compounds aggregate outside the carbon framework and grow to large rod with a diameter of 200 nm and a length of 600 nm due to the loser of confinement of mesoporous carbon. We also observed the individual huge rod (about 200 nm in diameter, length up to several microns) in Fig. 5e1. The amplification TEM image of the huge rod is shown in Fig. 5e3 and the lattice of huge rod is calculated to be ~ 0.39 nm, corresponding to the interplanar distance of WO_3 (001) facet. Fig. S4 is the SEM images of CW-10%-500 and CW-20%-500 films. Itôs obvious that the surface of the CW-10%-500 film is smooth, while there are long rods with size of 2 ±1 microns on the surface of CW-20%-500.

2.2 Ordered mesoporous C-WO_3 films calcinated at different temperatures

In order to investigate the effect of calcination temperature on ordering, graphitization degree and anticorrosion performance of the resulting mesoporous C-WO_3 films, we prepared four kinds of

ordered mesoporous C-WO_3 films by adjusting the calcination temperatures from 400 to 700 °C during heat treatment. The resulting products are labeled as CW-0%-y or CW-10%-y (y represents 400, 500, 600 or 700 °C). As shown in Fig. 6a and Fig. S5a, all samples display a strong diffraction peak at around 0.8-1.5°, and the diffraction peak shifts gradually towards higher degree with the rise of temperature. The result implies that the C-WO_3 films and pure C films possess thermally stable mesostructures, but the pore size in C-WO_3 films shrinks to some extent, especially the pure ordered mesoporous carbon (C-WO_3-0%). The wide-angle XRD patterns of CW-0%-y are shown in Fig. S5b, its diffraction peak moves from 19° to 23° with the rise of calcination temperature, indicating that the main part of CW-0%-y is amorphous carbon. The wide-angle XRD patterns of CW-10%-400 and CW-10%-500 films exhibit a broad diffraction peak at around 2ɗ = 19°, which is attributed to the amorphous carbon. However, the broad diffraction peak at 2ɗ of 19° becomes weak in CW-10%-600, and another broad diffraction peak at 2ɗ of 26°, which corresponds to (002) diffraction of typical graphite-like carbon phase,[58] appears in CW-10%-600 (shown in Fig. 6b). The results indicate that the C-WO_3 films have been partly graphitized during heat treatment at 600 °C, which is much lower than the graphitized temperature of pure ordered mesoporous carbon.[45] The relative low graphitized temperature of C-WO_3 is due to the existence of the tungsten compound, which can accelerate the phase transition from amorphous carbon to graphite. The tungsten compounds mainly consist of WO_3, and a small percentage of WC. The Raman spectra of CW-0%-y and CW-10%-y are given in Fig. S6 and Fig. 7. A distinct pair of broad bands show up at 1600 cm^{-1} (*G* band) and 1380 cm^{-1} (*D* band), respectively, when the calcination temperature increases over 600 °C. As shown in Table S1, we find that the I_D/I_G values of the samples decrease along with the incorporation of tungsten

compound or the increase of calcination temperature, suggesting the enhanced graphitization degree of carbon samples. The phenomenon suggests the improvement of graphitic structure in CW-0%-y and CW-10%-y films which is mainly due to the enhanced temperature during heat treatment. Meanwhile, compare the I_D/I_G values of CW-0%-y with the CW-10%-y in Table 1 and Table S1, we believe that tungsten compound arts as a catalyst for graphitization of amorphous carbon in CW-10%-y.

Fig. S7 and Fig. S8 show the static contact angles of CW-0%-y and CW-10%-y films, which can be used to estimate the surface hydrophilicity of C-WO_3 films. The related the static contact angle, surface energy and conductivity data are collected in Table S1. The static water contact angles of CW-0%-y films obviously increase with the calcination temperature from 54 to 81°. However, the static water contact angles of all CW-10%-y films are within the range of 50 ~ 65°, which do not obviously increase with the calcination temperature. The results show that the hydrophilicity of the CW-10%-y films is more associated with the content of tungsten oxide other than the treatment temperature. In addition, compared with the pure ordered mesoporous carbon (CW-0%-y), the electrical conductivity of the CW-10%-y films is multiplied along with the increase of heat treatment temperature.

Fig. 8 shows the N_2 adsorption-desorption isothermal curves and pore size distribution curves for CW-10%-y films. All of the CW-10%-y films illustrate typical IV type isotherms and H_1 hysteresis loop, indicating the mesoporous structure. However, with the increase of heat treatment temperature, CW-10%-y films also have a small hysteresis loop during relative pressure of 0.8 ~ 1.0 range, suggesting that the independent ordered mesoporous channels in C-WO_3 compounds are partially destroyed and lead to regional connected channels, which is consistent with the XRD

results in Fig. 6a. The pore structure parameters calculated through curves are concluded in Table 3. As we all know, thermal contraction could destroy the structure of mesoporous film, thus affecting its protective performance. We can see from Table 3 that the pore size of CW-10%-y films decreases along with the increase of calcination temperature. The pore size of CW-10%-700 film is only the half of CW-10%-400 film. The TEM images of CW-10%-y films are illustrated in Fig. 9. Itôs obvious that there are plenty of black tungsten oxide nanorods cross around the skeleton of mesoporous carbon. The diameters of tungsten oxide nanorods range from 40 to 80 nm in all CW-10%-y films, however, the length of tungsten oxide nanorods increases from several hundred nanometers to one micrometer along with the increase of heat treatment temperatures.

2.3 The forming process of WO_3 nanorod in ordered mesoporous carbon film

In order to analyze the elements of the ñthin-needlesò and the ñrod-shaped stuffò in TEM images, the elemental mapping images of CW-2.5%-600 and CW-10%-600 were obtained by STEM-EDS analysis. As shown in Fig. S9 and Fig. S10, both the ñthin-needlesò and the ñrod-shaped stuffò are tungsten compounds. Combined with the XPS (Fig. 1b), TEM (Fig. 5, Fig. S11) and wide-angle XRD analysis (Fig. 2b, Fig. S12), we can deduce that the ñthin-needlesò and ñthe rod-shaped stuffò (tungsten compounds) are in-fact tungsten oxide.

We selected the sample CW-10% to study the relationship between the structure and calcined temperature. After as-prepared CW-10% was heat polymerized at 100 ℃, you can see that silicotungstic acid with no specific morphology was uniformly dispersed in the F127-resol film (Fig. S11a,b). Then, CW-10%-100 was further calcined at 400 ℃, and F127 was cracked into the gaseous smaller molecules and left mesopores in carbon film and some micropores in the wall of carbon. Meanwhile, silicotungstic acid decomposed into tungsten oxide. We guess there is a

confinement effect on the growth of tungsten oxide. In other words, the directed mesopores could probably guide the growth of tungsten oxide, and in addition, the micropores would link up the nearby tungsten oxide. Therefore, we can see that tungsten oxide grew up in the form of rod with the confinement effect of porous structure. The tungsten oxide rod-shaped stuff was of 40 nm wide and 500 nm long (Fig. 9a). As the calcination temperature increased, tungsten oxide nanorods were induced to elongate in the ordered mesoporous frameworks and its length can reach 1εm (Fig. 9b,c,d). Fig. S11c,d are TEM images of CW-10%-600, and there are lots of black rods in ordered mesoporous skeleton. When we use HF acid to corrode CW-10%-600, we can obtain pure mesoporous carbon, which is named CW-C. As shown in Fig. S11e,f, the black rod-like parts disappeared, indirectly testifying that the black rod-shaped stuff is tungsten compound. Carbon can be removed from CW-10%-600 by heat treatment in air. The rest of the material is white, which is named the CW-W. From TEM images (Fig. S11g, h), we can see that there is only rod-like material without mesoporous structure. Its lattice is 0.385 nm, belonging to 001 of crystal WO_3, indicating that ordered mesoporous carbon skeleton has been removed. XRD Characterization (Fig. S12) also shows that most part of CW-W is WO_3, and only a small amount of component is WC.

In order to study the growth mechanism of the rod-shaped WO_3 inside the ordered mesopore, we prepared two referential samples. One is named as R1, which is fabricated by phenolic resin and silicotungstic acid without F127. The other is named as R2, which is fabricate by F127 and silicotungstic acid without phenolic resin. The precursors in R1 didnôt form regular micelle structure due to the absence of F127. As illustrated in Fig. S13, the phenolic resin and silicotungstic acid evenly dispersed in ethanol and were separately transformed into amorphous

carbon film and ruleless tungsten oxide particles after calcination. In the case of R2, although F127 would still self-assemble into regular rod-like micelle, tungsten oxide couldn't form ordered mesoporous structure in the absence of phenolic resin because of the easily agglomeration of tungsten oxide. The results show that, the F127 is able to form regular micelles and spontaneously co-assemble with phenolic resin and silicotungstic acid, then sacrifice to form micropores and mesopores during calcination. The role of the phenolic resin is to construct the carbon framework, confining and inducing the growth of the tungsten oxide.

Based on the above study, we simulated the formation process of ordered mesoporous C-WO_3 film and illustrated it in Fig. 10. In the beginning, the rod-shape micelles were formed from F127, phenolic resin precursor and silicotungstic acid. Then, the block copolymer F127 would be splitted into micromolecules during heat treatment at 350 ℃, which were finally volatized and left mesopore structure. Meanwhile, the polycondensation of phenolic resin would take place to obtain polymer network skeleton, and the silicotungstic acid would be pyrolyzed to be tungsten oxide. After being further calcinated at higher temperature, the polymer network skeleton is gradually carbonized and the tungsten compound in situ catalytically graphitizes amorphous carbon to graphitic structure. The oriented growth of tungsten oxide in the ordered mesoporous carbon skeleton can be clearly observed by adjusting the content of tungsten source. When tungsten source is low (2.5%), tungsten oxide nanoparticles separately and uniformly disperse in the mesoporous carbon skeleton. As the content of tungsten source increases to 5% ~ 10%, tungsten compounds aggregate together to be big rods due to the confinement of the mesoporous channel and the micropores in the wall of carbon skeleton. However, when tungsten source increases to 20%, the amount of tungsten source exceeds the limit of accommodation in the

mesoporous carbon skeleton. Therefore, the excessive tungsten compounds would grow to be a micron level black bulk without the restriction of mesoporous structure (Fig. 5e).

2.4 Electrochemical measurements of ordered mesoporous C-WO_3 film

As WO_3 and small amount of high conductive WC are in the skeleton of ordered mesoporous carbon, they can in situ catalyze graphitization of carbon, and improve the corrosion resistance and conductivity of carbon films. Fig. 11(a) shows the potentiodynamic polarization curves for ordered mesoporous C-WO_3 film-coated 304 SS after immersing in 0.5 mol L^{-1} H_2SO_4 aqueous solution for 1 h. The corrosion potential (E_{corr}) and corrosion current (i_{corr}) determined by potentiodynamic polarization extrapolations for these films are shown in Table S2. E_{corr} and I_{corr} for the ordered mesoporous carbon film-coated steel (CW-0%-500) are 91 mV (SCE) and 0.464 mA cm^{-2} respectively. When we introduce the WO_3 in mesoporous carbon, the E_{corr} increases for the ordered mesoporous C-WO_3 film-coated steel by about 70-140 mV (SCE). Wherein, CW-10%-500 displays the lowest corrosion current (0.0599 εA cm^{-2}), signifying the best corrosion resistance. We think that the introduction of corrosion-resistant WO_3 and SiO_2 with appropriate contents, may increase the contact angles with H_2SO_4, and not destroy the ordered mesoporous structure, and even enhance the stability with a perfect compact structure. However, when the content of WO_3 reaches to 20%, the ordered mesoporous structure has been disrupted, and the corresponding corrosion current is obviously higher than other mesoporous film.

Fig. S14 shows the potentiostatic polarization curve for ordered mesoporous C-WO_3 film-coated 304 SS in 0.5 mol L^{-1} H_2SO_4 solution. No degradation was observed after potentiostatic measurements for 4 h in CW-x-500 films except CW-20%-500, indicating their high stability at both cathode working potential and the anode working potential of PEMFC. The

electrochemical impedance spectra and the corresponding equivalent circuit of C-WO_3 films in 0.5 mol L^{-1} H_2SO_4 solution are shown in supporting information (Fig. S15 and Fig. S16), and the fitting parameters using Zview-impedance analysis software 2.80 are shown in Table S3. We can see that the charge-transfer resistance increases along with the enhanced content of WO_3, but the Warburg coefficient decreases. The phenomenon indicates that the introduction of WO_3 can significantly enhances the charge-transfer resistance and lowers the diffusion speed of corrosion products. However, when the content of WO_3 reach 20%, the parameters of CW-20%-500 become bad, due to the poor morphology and structure. Therefore, in order to get the good corrosion-resistant performance, the content of WO_3 should not exceed 20%.

Fig. 11(b,c) shows potentiodynamic polarization curves of pure ordered mesoporous carbon and ordered mesoporous C-WO_3 films suffering from different calcination temperatures in 0.5 M H_2SO_4 solution. The calculated corrosion current density (i_{corr}) and the corrosion potential (E_{corr}) from the curves are listed in Table S4. All of ordered mesoporous carbon and C-WO_3 films prepared at a low temperature (< 700 °C), show an excellent corrosion resistance. When the heat treatment is 700 °C, the violent shrinkage would happen in the carbon films and finally lead to a poor protection of the films that coated on the surface of the stainless steel.

According to the above research, we find out that carbon films can obtain the best anticorrosion performance and electrical conductivity when they are carbonized at 600 ℃. Therefore, we adopted CW-X%-600 films which were carbonized under 600 ℃ with different content of W as the support of Pt catalysts and investigated their electrocatalytic performance. The hydrogen adsorption-desorption data recorded by cyclic voltammetry (CV) with a traditional three electrode system in 0.5 mol L^{-1} H_2SO_4 aqueous solution are shown in Fig. 11d. The CV curve of

Pt/CW-0%-600 catalyst presents a pair of cathodic and anodic peaks between -0.2 ~ 0 V (SCE), which is a typical behavior of hydrogen adsorption and desorption on Pt surface in acidic medium.[59,60] However, in the case of Pt/CW-2.5%-600, Pt/CW-5%-600, Pt/CW-10%-600 and Pt/CW-20%-600 catalysts, the redox peaks in CV curves gradually shift towards higher voltage along with the enhanced incorporation of W in carbon films. As reported by previous research, the redox peak of pure WO_3 in acidic electrolyte is located at 0.1V (v.s SCE).[61] Thus, the peak shifts can be explained by the co-catalysis between Pt and WO_3. We use hydrogen desorption peak current density (I_{max}) and electrochemical active surface areas (E_{SA}) calculated from hydrogen desorption peaks to evaluate the electrocatalytic activities of catalysts and conclude these data in Table 4. Itôs obvious that the electrocatalytic performance of Pt/CW-X%-600 is improved after incorporating W. For example, the I_{max} and E_{SA} of Pt/CW-10%-600 is 9.2 mA cm^{-2} and 65.7 m^2 g^{-1}, respectively, much higher than that of Pt/CW-0%-600 (4.0 mA cm^{-2} and 6.7 m^2 g^{-1}). The distinguished improved electrochemical activities mainly originate from follows reasons: First of all, although the pure ordered mesoporous carbon possesses a relative high surface area, it has a low electron conductivity and poor hydrophilicity. Thus, researchers usually modify the pure ordered mesoporous carbon by surface modification with CTAB, nitrogen doping and metal composition.[62-64]

It has been proved by many studies that the presence of WO_3 species can ameliorate the hydrophilicity of carbon surface, leading to a better Pt anchoring and dispersion. Secondly, amorphous carbon has been partially catalytically graphitized by W compound nanoparticles during calcination, resulting in a better graphitic crystallinity and electron conductivity. Finally, WO_3 is able to accept proton by forming a nonstoichiometric H_xWO_3 compound in acidic system

and this spillover of hydrogen onto the surface of H_xWO_3 compound will free the Pt sites for further chemisorption of hydrogen molecules. This assistant catalysis accelerates the oxidation reaction and has been indirectly proved by the redox peak shifts in CV curves.[65] However, when the mass content of W is up to 20%, the ordered mesoporous structure of carbon has been destroyed during calcination at 500 ℃ (shown in Fig. 2a) and cannot effectively help the dispersing WO_3. Consequently, Pt/CW-10%-600, which has been modified by suitable content of W, presents the most excellent elctrocatalytic performance due to the concerted catalysis between Pt and WO_3, improved electron conductivity and suitable mesoporous structures. Fig. 11e shows the cyclic voltammetry of the Pt/CW-x-600 samples toward methanol oxidation in 2.0 mol L^{-1} CH_3OH + 1.0 mol L^{-1} H_2SO_4 solution. Their methanol oxidation peaks are located at about 0.73 V (SCE), and their peak current densities are 8.0, 10.5, 14.1, 43.1 and 19.9 mA cm^{-2}, respectively. Among all catalysts, Pt/CW-10%-600 exhibits the lowest initial oxidation potential and highest peak current density of methanol oxidation, implying their best elctrocatalytic performance.

3. Conclusions

We developed a simple self-assembly route to prepare ordered mesoporous C-WO_3 nanocomposites. Tungsten oxide grew up in the form of rod due to the confinement effect of porous structure. The resulting ordered mesoporous nanocomposites possess a large surface area, excellent corrosion resistance, improved graphitization degree and hydrophilicity. Consequently, the ordered mesoporous C-WO_3 nanocomposites work as electrocatalysts carrier of PEMFC show more superior electrocatalytic activies than pure ordered mesoporous carrier.

4. Experimental Section

4.1 Chemical materials

Triblock copolymer Pluronic F127 (Mw = 12600, $PEO_{106}PPO_{70}PEO_{106}$, EO= ethylene oxide, PO=propylene oxide) was purchased from Sigma-Aldrich Corporation. Phenol (C_6H_6O), formaldehyde solution (HCHO, 37 wt%), silicotungstic acid ($H_4SiW_{12}O_{40}$), sodium hydroxide (NaOH), hydrochloric acid (HCl, 37 wt%), sulfuric acid (H_2SO_4), methanol (CH_3OH) and ethanol (C_2H_5OH) were purchased from Shanghai Chemical Corporation. All chemicals were used as received without any further purification. Distilled water was used in all experiments. The low-molecular-weight resol (phenol-formaldehyde, Mw < 500, 20 wt% in ethanol) as a carbon source was prepared according to the procedure reported by the Zhao group.[66]

4.2 Synthesis of ordered mesoporous C-WO_3 films

In a typical synthesis of ordered mesoporous C-WO_3 film, 1.0 g of triblock copolymer Pluronic F127 was poured into 15.0 mL of ethanol with vigorous stirring at 40 ℃ to obtain a clear solution A. Meanwhile, a certain amount of silicotungstic acid was dissolved in 5.0 mL of ethanol with vigorous stirring at room temperature to obtain a clear solution B. Then, 5.0 g of resol (20 wt% in ethanol) was added in solution A and the mixture was stirred for 10 min. Next, solution B was dripped slowly into solution A with vigorous stirring to obtain a homogeneous precursor solution. The film was fabricated by spin-coating the solution onto clean type 304 stainless steel at 1500 rpm for 60 s using a spin coater (KW-4A), the same process was repeated for 5 times. The film was aged at room temperature for 24 h and then thermopolymerized in an oven at 100 ℃ for 24 h. The result yellow deposit was carbonized in a tubular furnace at 350 ℃ for 3 h, and then at 400, 500, 600 or 700 ℃ for 2 h respectively, with a heating rate of 1 ℃ min^{-1} under N_2 atmosphere. Ordered C-WO_3 carbon film was obtained and denoted as CW-x-y, where x represented the percent content of tungsten oxide in composite film, y represents the calcination

temperature. When the x is 0, the mesoporous film is named CW-0%, which means pure ordered mesoporous carbon film without tungsten oxide. The ordered mesoporous films with different compositions in a wide range from 0 to 20% of tungsten oxide were prepared by varying the content of silicotungstic acid.

In order to explore the growth process and influencing factors of tungsten compound, we prepared the following samples: (1) the sample was prepared like CW-10%-500, except without F127, denoted as R-1; (2) the sample was prepared like CW-10%-500, except without resol, denoted as R-2; (3) CW-10%-600 was calcinated in air at 550 ℃ to remove carbon, denoted as CW-WO_3; (4) CW-10%-600 was washed with 10 % hydrofluoric acid solution to remove WO_3, denoted as CW-C.

4.3 Deposit Pt on the ordered mesoporous C-WO_3 nanocomposites

Pt deposited on ordered mesoporous C-WO_3 nanocomposites were fabricated by ethylene glycol reduction method with microwave-assisted technology.[48] Firstly, grind ordered mesoporous film into powder. Secondly, 1.4 mL of 0.038 mol L^{-1} H_2PtCl_6 ethylene glycol solution and 20 mL of ethylene glycol were mixed well, followed by adjusted the pH to 9 by using NaOH ethylene glycol solution (2.5 mol L^{-1}). Then, 40 mg of ordered mesoporous nanocomposite was added to the mixture, and ultrasonicated for 30 min. The mixture was placed in a microwave oven and irradiated for 120 s at 700 W. At last, the Pt catalysts were centrifuged and washed with deionized water and ethanol several times, and dried in a vacuum at 80 ℃ oven overnight. The prepared electrocatalysts were assigned as Pt/CW-x-y, and the nominal loading of Pt was 20 wt%.

4.4 Structure and performance characterization

X-ray photoelectron spectroscopy (XPS) was conducted on PHI 5000 Versaprobe apparatus

(ULVAC-PH Japan). X-ray diffraction (XRD) patterns were obtained using a Bruker D8 Advance diffractometer using a Cu Ka source (ƛ = 0.154056 nm) at 40 kV and 40 mA. Raman spectra were obtained with a French JY HR800 microscopic Raman system, using a He-Ne laser at an excitation wavelength of 633 nm. Nitrogen adsorption-desorption isotherms were measured at 77 K using a Micromeritics ASAP 2010 instrument. The specific surface areas were calculated by utilizing the Brunauer-Emmett-Teller (BET) method based on adsorption data. The pore size distributions derived from the adsorption branches of isotherms were estimated based on the Barrett-Joyner-Halenda (BJH) model. Water contact angles were measured by a contact angle system SL200B (SOLON. Tech., China). The in-plane electrical conductivity was measured by the Wentworth Laboratories 6514 System Electrometer Keithley. Transmission electron microscopy (TEM) experiments and selected area electron diffraction (SAED) pattern were conducted by a FEI Tecnai G2 system operated at 200 kV. The samples for TEM measurements were suspended in ethanol and supported on a holey carbon film on a Cu grid. Energy dispersive X-ray spectrum (EDS) installed in FEI Tecnai G2 system was also used to analyze the microzone composition (STEM-EDS mapping) of the sample. The scanning electron microscopy (SEM) images were recorded on a Quanta 200 microscope with an accelerating voltage of 20 kV, to observe the surface of the films.

4.5 Corrosion behavior

Electrochemical experiments were carried out in a beaker using a standard three-electrode cell with a coated or uncoated 304 SS sheet as working electrode, a saturated calomel electrode (SCE) as reference electrode, and a platinum foil as counter electrode in 0.5 mol L^{-1} H_2SO_4. For all working electrodes a surface area of 1 cm^2 has been considered. Due to the fact that each working

electrode has been coated only on one side, the uncoated face and the edges have been protected from the acid solution with an epoxy resin. An electrochemical interface (Solartron 1287) was employed to conduct potentiodynamic polarization measurements at a scan rate of 10 mV s^{-1}. Potentiostatic polarizations were conducted on a Solartron 1287, to investigate the performance and stability of the films, the polarizations were recorded at applied anode potential of -0.1 V (SCE) and cathode potential 0.6 V (SCE) for PEMFC. Potentiostatic polarizations were conducted at room temperature. Electrochemical impedance spectroscopy (EIS) measurements using Solartron 1260 frequency response analyzer coupled to Solartron 1287 potentiostat were obtained at frequencies between 100 kHz and 0.01 Hz. The amplitude of the sinusoidal potential signal was 5 mV.

4.6 Electrocatalytic measurements

Cyclic voltammetry (CV) measurement was conducted on a CHI660C electrochemical workstation with a conventional three-electrode cell, in 0.5 mol L^{-1} H_2SO_4 between -0.22 and 0.98 V (SCE) with a scan rate of 20 mV s^{-1} and in 2.0 mol L^{-1} CH_3OH + 1.0 mol L^{-1} H_2SO_4 between 0 V and 1 V (SCE) at the same scan rate. Platinum foil electrode and a SCE were used as the counter electrode and reference electrode, respectively. The electrocatalyst supported on polished glassy carbon (GC) electrode as working electrode was prepared as follows: 5 mg of the prepared electrocatalyst mixed with 1 mL ethanol and 50 εL of 5 wt% Nafion solutions (Du Pont) was sonicated for 30 min to obtain inky slurry. Then, 25εL of the slurry was dropped on the surface of the GC electrode to form a thin layer (0.1256 cm^2).

Acknowledgements

The authors appreciate the financial support from the National Natural Science Foundation of

China (51372115).

Notes and references

[a]*College of Material Science and Technology, Nanjing University of Aeronautics and Astronautics, Nanjing 210016 (P.R. China), Fax: (+86) 25 52112626*

E-mail: jianph@nuaa.edu.cn

[b]*Department of Nanoscience and Nanoengineering, Faculty of Science and Engineering, Waseda University, 3-4-1 Okubo, Shinjuku, Tokyo 169-8555 (Japan)*

[c]*China Key Laboratory of Renewable Energy and Gas Hydrate, Guangzhou Institute of Energy Conversion, Chinese Academy of Sciences, Guanzhou 510640 (P.R. China)*

ÀElectronic Supplementary Information (ESI) available: Additional structural characterizations and electrochemical measurements. See DOI:

1. S. Gottesfeld and T. Zawodzinski, Adv. Electrochem. Sci. Eng., 1997, 5, 195-301.

2. V. Mehta and J. S. Cooper, J. Power Sources, 2003, 1, 32-53.

3. P. Costamagna and S. Srinivasan, J. Power Sources, 2001, 1-2, 242-252.

4. T. V. Nguyen and R. E. White, J. Electrochem. Soc., 1993, 8, 2178-2186.

5. M. Lefèvre, E. Proietti, F. Jaouen and J. P. Dodelet, Science, 2009, 324, 71-746

6. K. P. Gong, F. Du, Z. H. Xia, M. Durstock and L. M. Dai, Science, 2009, 323, 760-764.

7. L. S. Panchakarla, K. S. Subrahmanyam, S. K. Saha, A. Govindaraj, H. R. Krishnamurthy, U. V. Waghmare and C. N. R. Rao, Adv. Mater., 2009, 21, 4726-4730.

8. P. J. Kulesza and L. R. Faulkner, J. Am. Chem. Soc., 1988, 110, 4905-4913.

9. X. Z. Cui, J. L. Shi, H. R. Chen, L. X. Zhang, L. M. Guo, J. H. Gao and J. B. Li, J. Phys. Chem.

B, 2008, 112, 12024-12031.

10. B. S. Hobbs and A. C. C. Tseung, Nature, 1969, 222, 556-558.
11. C. T. Kresge, M. E. Leonowicz, W. J. Roth, J. C. Vartuli and J. S. Beck, Nature, 1992, 6397, 710-712.
12. D. Y. Zhao, J. L. Feng, Q. S. Huo, N. Melosh, G. H. Fredrickson, B. F. Chmelka and G. D. Stucky, Science, 1998, 5350, 548-552.
13. M. E. Davis, Nature, 2002, 6891, 813-821.
14. P. D. Yang, D. Y. Zhao, D. I. Margolese and G. D. Stucky, Nature, 1998, 6707,152-155.
15. H. F. Bao, J. P. Yang, Y. Huang, Z. P. Xu, N. Hao, Z. X. Wu, G. Q. Lu and D. Y. Zhao, Nanoscale, 2011, 3, 4069-4073.
16. S. Y. Choi, M. Mamak, N. Coombs, N. Chopra and G. A. Ozin, Adv. Funct. Mater., 2004, 4, 335-344.
17. X. F. Jiang, B. P. Bastakoti, W. Weng, T. Higuchi, H. Oveisi, N. Suzuki, W. J. Chen, Y. T. Huang and Y. Yamauchi, Chem. Eur. J., 2013, 19, 10958-10964.
18. X. P. Fang, B. K. Guo, Y. F. Shi, B. Li, C. X. Hua, C. H. Yao, Y. C. Zhang, Y. S. Hu, Z. X. Wang and G. D. Stucky, Nanoscale, 2012, 4, 1541-1544.
19. S. H. Joo, S. J. Choi, I. Oh, J. Kwak, Z. Liu, O. Terasaki and R. Ryoo, Nature, 2001, 6843, 169-172.
20. G. W. Zhao, J. P. He, C. X. Zhang, J. H. Zhou, X. Chen and T. Wang, J. Phys. Chem. C, 2008, 4, 1028-1033.
21. G. S. Chai, S. B. Yoon, J. S. Yu, J. H. Choi and Y. E. Sung, J. Phys. Chem. B, 2004, 22, 7074-7079.

22. Y. Ye, C. Jo, I. Jeong and J. Lee, Nanoscale, 2013, 5, 4584-4605.

23. J. Tang, T. Wang, X. C. Pan, X. Sun, X. L. Fan, Y. X. Guo, H. R. Xue and J. P. He, J. Phys. Chem. C, 2013, 117, 16896-16906.

24. P. J. Ferreira, G. J. Ia O', Y. Shao-Horn, D. Morgan, R. Makharia, S. Kocha and H. A. Gasteiger, J. Electrochem. Soc., 2005, 11, 2256-2271.

25. S. Y. Huang, P. Ganesan P, S. Park and B. N. Popov, J. Am. Chem. Soc., 2009, 39, 13898-13899.

26. A. F. Gross, M. R. Diehl, K. C. Beverly, E. K. Richman and Sarah H. Tolbert, J. Phys. Chem. B, 2003, 107, 5475-5482.

27. A. Takai, Y. Doi, Y. Yamauchi and K. Kuroda, J. Phys. Chem. C, 2010, 114, 7586-7593.

28. H. F. Yang, Q. Y. Lu, F. Gao, Q. H. Shi, Y. Yan, F. Q. Zhang, S. H. Xie, B. Tu and D. Y. Zhao, Adv. Funct. Mater., 2005, 15, 1377-1384.

29. D. L. Li, H. S. Zhou and I. Honma, Nat. Mater., 2003, 3, 65-72.

30. S. H. Joo, Jeong Y. Park, C. K. Tsung, Y. Yamada, P. D. Yang and G. A. Somorjai, Nat. Mater., 2009, 8, 126-131.

31 Z. K. Sun, B. Sun, M. H. Qiao, J. Wei, Q. Yue, C. Wang, Y. H. Deng, S. Kaliaguine and D. Y. Zhao, J. Am. Chem. Soc., 2012, 134, 17653-17660.

32. D. Rats, J. Sevely, L. Vandenbulcke, R. Benoit, R. Erre, V. Serin and J. Sevely, Thin Solid Films, 1995, 1-2, 177-183.

33. R. Bertoncello, A. Casagrande, M. Casarin, A. Glisenti, E. Lanzoni, L. Mirenghi and E. Tondello, Surf. Interface Anal., 1992, 7, 525-531.

34. G. Leclercq, M. Kamal, J. F. Lamonier, L. Feigenbaum, P. Malfoy and L. Leclercq, Appl. Catal.

A-Gen., 1995, 2, 169-190.

35. N. Moncoffre, G. Hollinger, H. Jaffrezic, G. Marest and J. Tousset, Nuclear Instruments and Methods in Physics Research B, 1985, 7-8, 177-183.

36. L. N. Bùi, M. Thompson, N. B. Mckeown, A. D. Romaschin and P. G. Kalman, Analyst, 1993, 118, 463-474.

37. S. Contarini, S. P. Howlett, C. Rizzo, B. A. De Angelis, Appl. Surf. Sci., 1991, 3-4, 177-183.

38. L. Ramqvist, K. Hamrin, G. Johansson, A. Fahlman and C. Nordling, J. Phys. Chem. Solids, 1969, 7, 1835-1847.

39. N. M. Mackie, D. G. Castner and E. R. Fisher, Langmuir, 1998, 5, 1227-1235.

40. N. Shohoji, P. M. Amaral, J. C. Fernandes, L. G. Rosa, D. Martínez and J. Rodríguez, Mater. T. Jim, 2000, 1, 246-249.

41. S. Kumar, D. R. Chopra, G. C. Smith, J. Vac. Sci. Technol. B, 1992, 3, 1218-1220.

42. C. D. Wagner, J. F. Moulder, L. E. Davis, J. F. Moulder and G. E. muilenberg, Handbook of X-ray photoelectron spectroscopy, Perking-Elmer Corporation, Physical Electronics Division, USA 1979.

43. Y. Meng, D. Gu, F. Q. Zhang, Y. F. Shi, L. Cheng, D. Feng, Z. X. Wu, Z. X. Chen, Y. Wan, A. Stein and D. Y. Zhao, Chem. Mater., 2006, 18, 4447-4464.

44. T. Wang, C. X. Zhang, X. Sun, Y. X. Guo, H. Guo, J. Tang, H. R. Xue, M. Z. Liu, X. X. Zhang, L. Zhu, Q. Q. Xie and J. P. He, J. Power Sources, 2012, 212, 1-12.

45. X. Q. Wang, C. D. Liang and S. Dai, Langmuir, 2008, 24, 7500-7505.

46. Y. Hanzawa, H. Hatori, N. Yoshizawa and Y. Yamada, Carbon, 2002, 40, 575-581.

47. E. I. Ross-Medgaarden and I. E. Wachs, J. Phys. Chem. C, 2007, 111, 15089-15099.

48. A. Baserga, V. Russo, F. Di Fonzo, A. Bailini, D. Cattaneo, C. S. Casari, A. Li Bassi and C. E. Bottani, Thin Solid Films, 2007, 515, 6465-6469.

49. W. Wu, Q. Yu, J. Lian, J. Bao, Z. Liu and S. S. Pei, J. Cryst. Growth, 2010, 312, 3147-3150.

50. A. C. Ferrari and J. Robertson, Phys. Rev. B, 2000, 61, 14095-14107.

51. Z. Yan, G. He, P. K. Shen, Z. Luo, J. Xie and M. Chen, J. Mater. Chem. A, 2014, 2, 4014-4022.

52. W. Weisweiler, N. Subramanian and B. Terwiesch, Carbon, 1971, 9, 755-758.

53. A. æya and S. ætani, Carbon, 1979, 17, 131-137.

54. W. Weeisweiler, N. Subramanian and B. Terwiesch, Carbon, 1971, 9, 755-761.

55. I. Mochida, R. Ohtsubo and K. Takeshita, Carbon, 1980, 18, 25-30.

56. A. æya and H. Marsh, J. Mater. Sci., 1982, 17, 309-322.

57. D. Y. Zhao, J. L. Feng, Q. S. Huo, N. Melosh, G. H. Fredrickson, B. F. Chmelka and G. D. Stucky, Science, 1998, 279, 548-552.

58. M. Sevilla and A. B. Fuertes, Carbon, 2006, 44, 468-474.

59. S. Jayaraman, T. F. Jaramillo, S. H. Baeck and E. W. McFarland, J. Phys. Chem. B, 2005, 109, 22958-22966.

60. X. Z. Cui, L. M. Guo, F. M. Cui, Q. J. He and J. L. Shi, J. Phys. Chem. C, 2009, 113, 4134-4138.

61. S. H. Yoon, E. Kang, J. K. Kim, C. W. Lee and J. W. Lee, Chem. Commun., 2011, 47, 1021-1023.

62. J. H. Zhou, J. P. He, Y. J. Ji, W. J. Dang, X. L. Liu, G. W. Zhao, C. X. Zhang, J. S. Zhao, Q. B. Fu and H. P. Hu, Electrochim. Acta, 2007, 14, 4691-4695.

63. J. H. Zhou, J. P. He, T. Wang, D. Sun, G. W. Zhao, X. Chen, D. J. Wang and Z. Y. Di, J. Mater.

Chem., 2008, 47, 5776-5781.

64. R. L. Liu, D. Q. Wu, X. L. Feng and K. Müllen, Angew. Chem. Int. Edit., 2010, 14, 2565-2569.

65. J. Zhang, J. P. Tu, G. H. Du, Z. M. Dong, Q. M. Su, D. Xie and X. L. Wang, Electrochimi. Acta, 2013, 88, 107-111.

66. Y. Meng, D. Gu, F. Q. Zhang, Y. F. Shi, H. F. Yang, Z. Li, C. Z. Yu, B. Tu and D. Y. Zhao, Angew. Chem. Int. Ed., 2005, 44, 7053-7059.

Figure Captions

Fig. 1 XPS spectrum of CW-0%-500 and CW-10%-500: (a) C_{1s}, (b) W_{4f}

Fig. 2 (a) Small-angle XRD and (b) wide-angle XRD patterns of ordered mesoporous C-WO_3 films.

Fig. 3 Raman spectra of ordered mesoporous CW-x-500 films.

Fig. 4 N_2 adsorption-desorption isotherm (a) and pore size distribution (b) of ordered mesoporous C-WO_3 films. For clarity, the isotherms (a) for the CW-2.5%-500, CW-5%-500, CW-10%-500, CW-20%-500 are offset vertically by 100, 200, 300, 400 $cm^3\ g^{-1}$, respectively. The isotherms (b) for the CW-2.5%-500, CW-5%-500, CW-10%-500, CW-20%-500 are offset vertically by 0.05, 0.10, 0.15, 0.20 $cm^3\ g^{-1}\ nm^{-1}$, respectively.

Fig. 5 TEM images of ordered mesoporous C-WO_3 films: (a) CW-0%-500, (b) CW-2.5%-500, (c) CW-5%-500, (d) CW-10%-500 and (e) CW-20%-500

Fig. 6 (a) Small-angle XRD and (b) wide-angle XRD patterns of CW-10%-y films, y represents the calcination temperature.

Fig. 7 Raman spectra of ordered mesoporous CW-10%-y films.

Fig. 8 N_2 adsorption-desorption isotherm (a) and pore size distribution (b) of CW-10%-y films.

Fig. 9 TEM images of ordered mesoporous C-WO_3 films: (a) CW-10%-400, (b) CW-10%-500, (c) CW-10%-600, and (d) CW-10%-700.

Fig. 10 Schematic illustration of the formation process of highly oedered mesoporous C-WO_3 films

Fig. 11 Potentiodynamic polarization curves of ordered mesoporous CW-x-500 (a), CW-0%-y films (b) and CW-10%-y films (c) in 0.5 mol L^{-1} H_2SO_4 solution. CV curves of Pt/CW-0%-600,

Pt/CW-2.5%-600, Pt/CW-5%-600, Pt/CW-10%-600 and Pt/CW-20%-600 samples in 0.5 mol L^{-1} H_2SO_4 (d) and 2.0 mol L^{-1} CH_3OH + 1.0 mol L^{-1} H_2SO_4 (e) with a scan rate of 20 mv s^{-1}

Table Captions

Table 1 The values of contact angles with water, electrical conductivity and I_D/I_G for the mesoporous C-WO_3 films.

Table 2 Structural parameters of ordered mesoporous C-WO_3 films.

Table 3 Structural parameters of CW-10%-y films.

Table 4 Electrochemical parameters of the Pt/CW-x-600 samples obtained from CV curves in 0.5 mol L^{-1} H_2SO_4 and 2.0 mol L^{-1} CH_3OH + 1.0 mol L^{-1} H_2SO_4 with a scan rate of 20 mv s^{-1}.

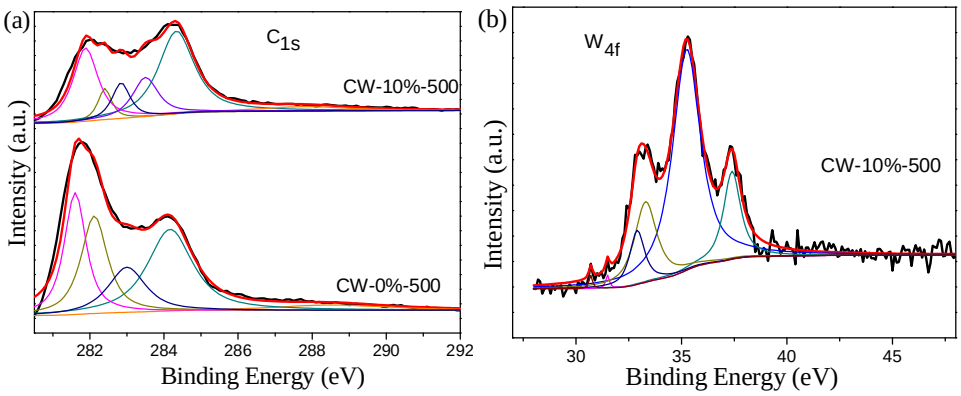

Fig. 1 XPS spectrum of CW-0%-500 and CW-10%-500: (a) C_{1s}, (b) W_{4f}

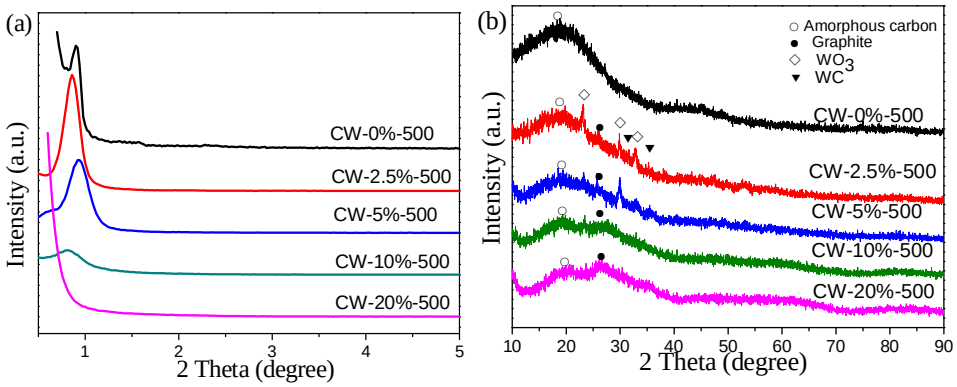

Fig. 2 (a) Small-angle XRD and (b) wide-angle XRD patterns of ordered mesoporous C-WO_3 films.

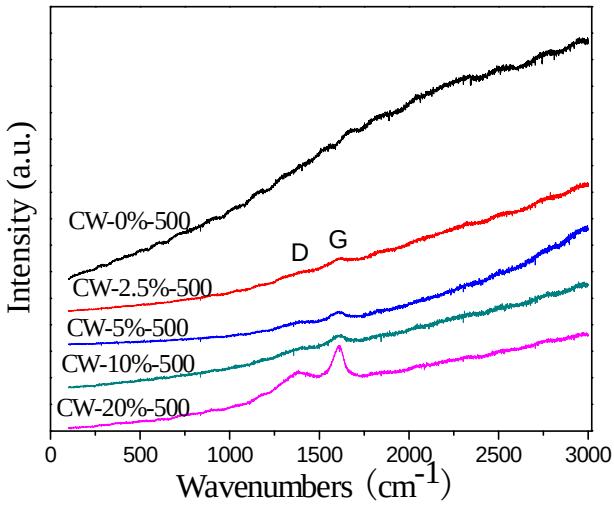

Fig. 3 Raman spectra of ordered mesoporous CW-x-500 films.

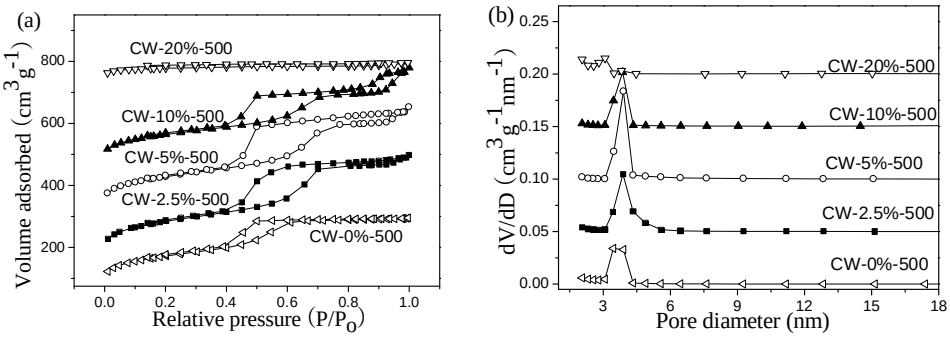

Fig. 4 N_2 adsorption-desorption isotherm (a) and pore size distribution (b) of ordered mesoporous C-WO_3 films. For clarity, the isotherms (a) for the CW-2.5%-500, CW-5%-500, CW-10%-500, CW-20%-500 are offset vertically by 100, 200, 300, 400 cm^3 g^{-1}, respectively. The isotherms (b) for the CW-2.5%-500, CW-5%-500, CW-10%-500, CW-20%-500 are offset vertically by 0.05, 0.10, 0.15, 0.20 cm^3 g^{-1} nm^{-1}, respectively.

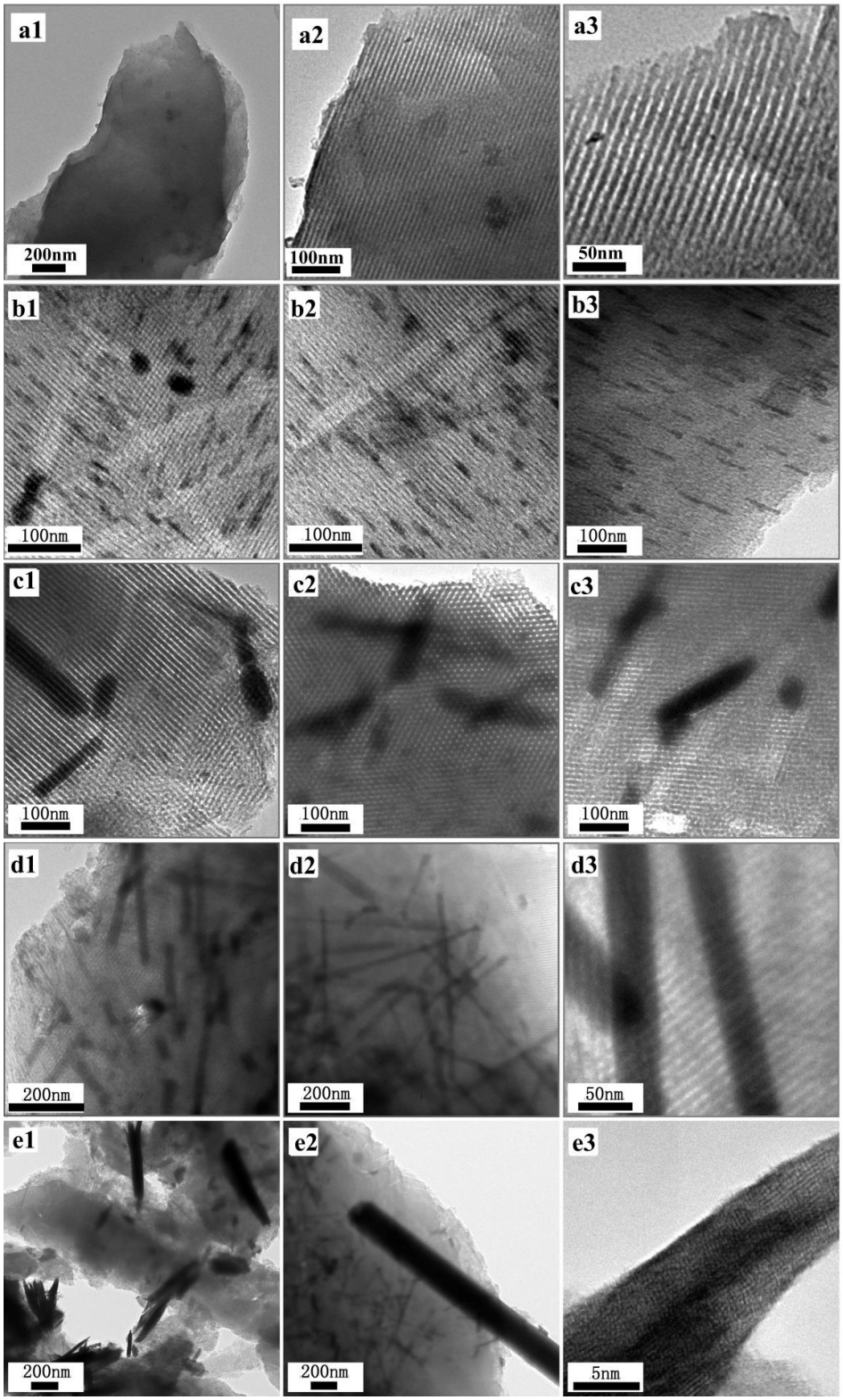

Fig.5 TEM images of ordered mesoporous C-WO_3 films: (a) CW-0%-500, (b) CW-2.5%-500, (c) CW-5%-500, (d) CW-10%-500 and (e) CW-20%-500

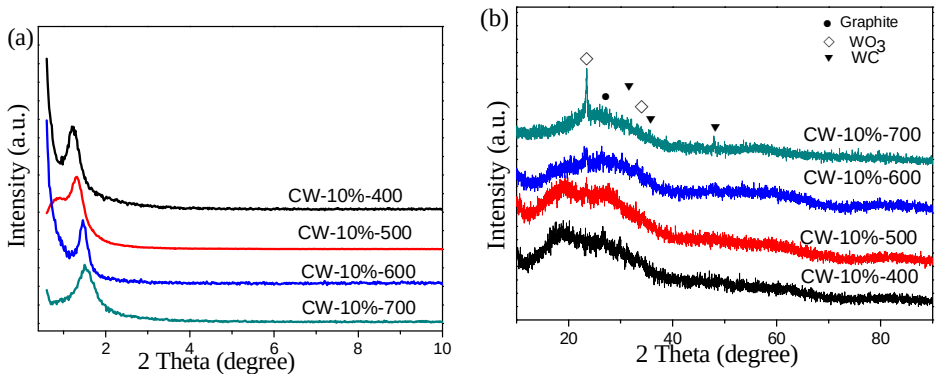

Fig. 6 (a) Small-angle XRD and (b) wide-angle XRD patterns of CW-10%-y films, y represents the calcination temperature.

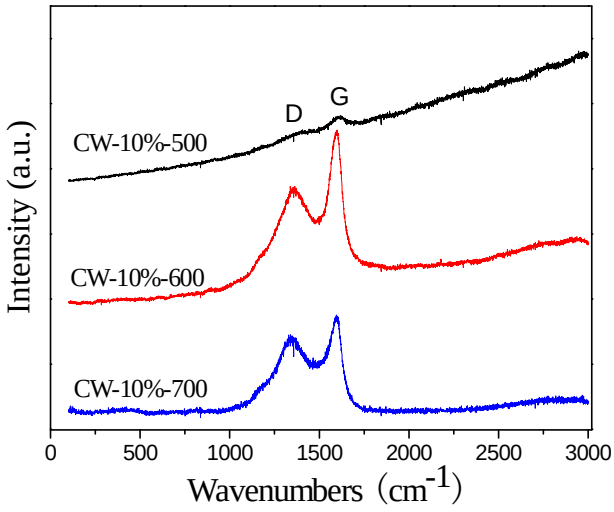

Fig. 7 Raman spectra of ordered mesoporous CW-10%-y films.

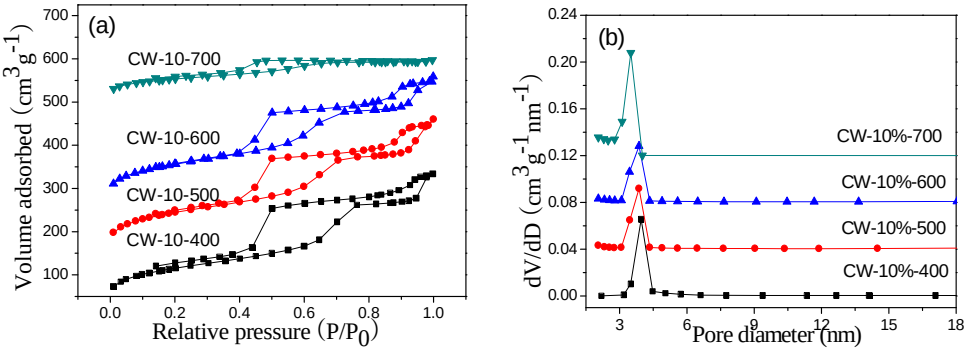

Fig. 8 N_2 adsorption-desorption isotherm (a) and pore size distribution (b) of CW-10%-y films.

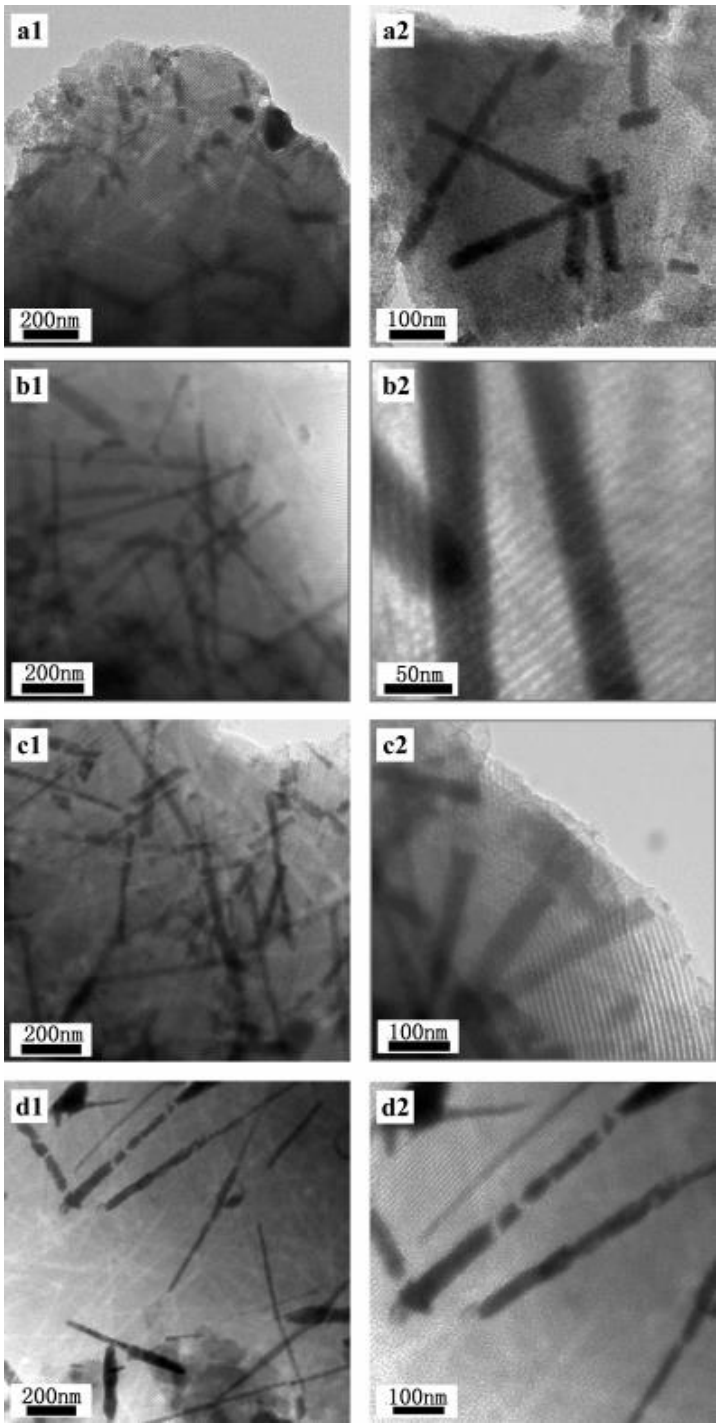

Fig. 9 TEM images of ordered mesoporous C-WO_3 films: (a) CW-10%-400, (b) CW-10%-500, (c) CW-10%-600, and (d) CW-10%-700.

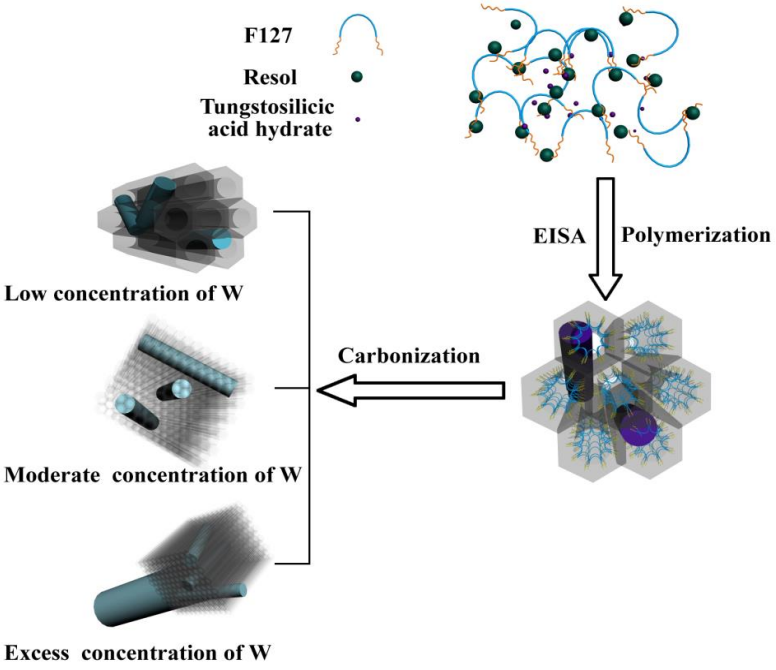

Fig. 10 Schematic illustration of the formation process of highly oedered mesoporous C-WO_3 films.

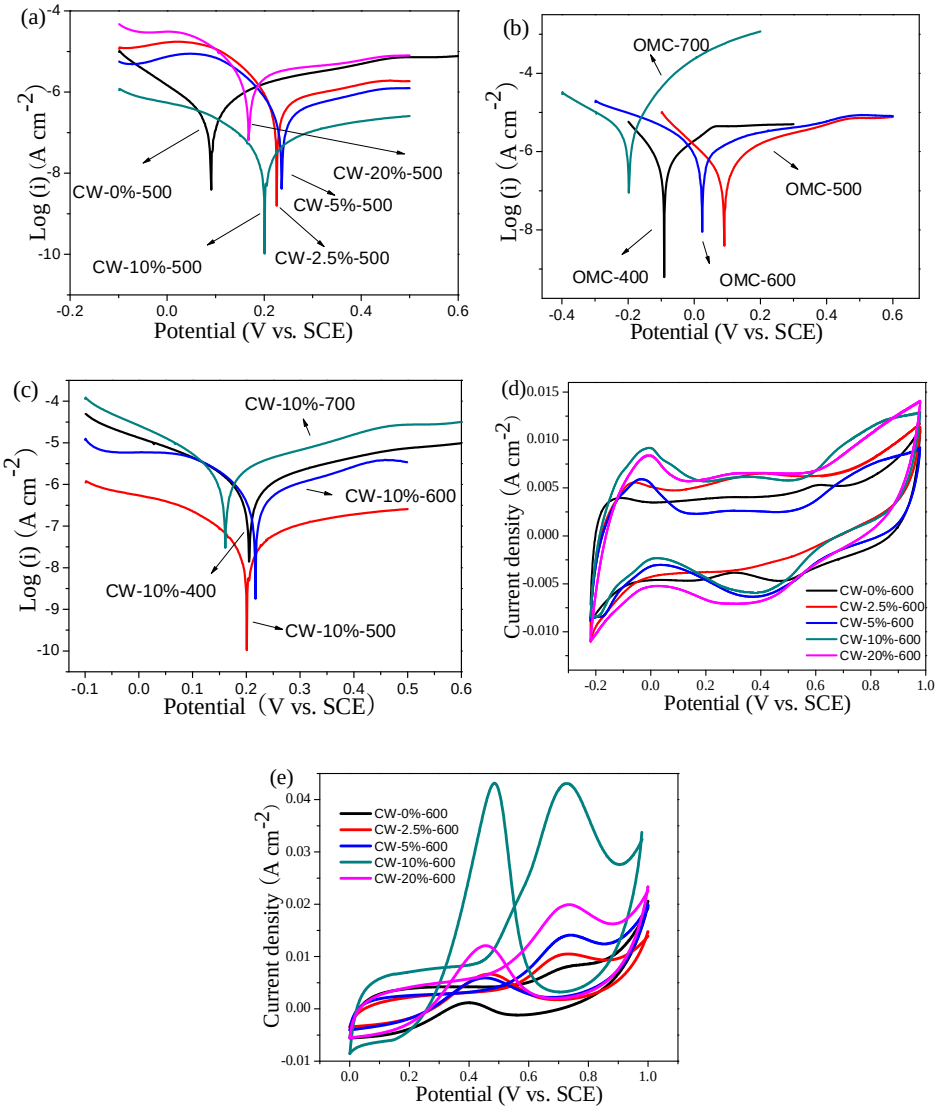

Fig. 11 Potentiodynamic polarization curves of ordered mesoporous C-WO_3-x-500 (a), CW-0%-y films (b) and CW-10%-y films (c) in 0.5 mol L^{-1} H_2SO_4 solution. CV curves of Pt/ CW-0%-600, Pt/ CW-2.5%-600, Pt/ CW-5%-600, Pt/ CW-10%-600 and Pt/ CW-20%-600 samples in 0.5 mol L^{-1} H_2SO_4 (d) and 2.0 mol L^{-1} CH_3OH + 1.0 mol L^{-1} H_2SO_4 (e) with a scan rate of 20 mv s^{-1}

Table 1 The values of contact angles with water, electrical conductivity and I_D/I_G for the mesoporous C-WO_3 films.

Sample	Contact angle (°)	Surface energy (N m^{-2})	G (S m^{-1})	I_D/I_G
CW-0%-500	71	32.0	0.0043	-
CW-2.5%-500	65	37.1	0.061	5.69
CW-5%-500	65	37.2	0.062	3.23
CW-10%-500	62	39.5	0.080	1.84
CW-20%-500	61	40.2	0.82	1.16

Table 2 Structural parameters of ordered mesoporous C-WO_3 films.

Sample	S_{BET} (m^2 g^{-1})	V_{total} (cm^3 g^{-1})	R_{meso} (%)	D (nm)
CW-0%-500	588	0.46	76.1%	3.1
CW-2.5%-500	631	0.61	83.6%	3.9
CW-5%-500	607	0.62	83.5%	4.1
CW-10%-500	558	0.59	82.7%	4.2
CW-20%-500	190	0.12	50.2%	2.5

Table 3 Structural parameters of CW-10%-y films.

Sample	S_{BET} (m^2 g^{-1})	V_{total} (cm^3 g^{-1})	R_{meso} (%)	D (nm)
CW-10%-400	402	0.52	92.2%	5.1
CW-10%-500	558	0.59	82.6%	4.2
CW-10%-600	626	0.60	76.1%	3.8
CW-10%-700	469	0.29	47.7%	2.5

Table 4 Electrochemical parameters of the Pt/CW-x-600 samples obtained from CV curves in 0.5 mol L^{-1} H_2SO_4 and 2.0 mol L^{-1} CH_3OH + 1.0 mol L^{-1} H_2SO_4 with a scan rate of 20 mv s^{-1}.

samples	I_{max}[a] (mA cm^{-2})	Q_H[a] (mC)	S_{EA}[a] (m^2 g^{-1})	Forward peak current density of methanol oxidation[b] (mA cm^{-2})
Pt/ CW-0%-600	4.0	0.33	6.7	8.0
Pt/CW-2.5%-600	5.6	0.47	9.3	10.5
Pt/ CW-5%-600	5.9	3.16	63.3	14.1
Pt/CW-10%-600	9.2	3.28	65.7	43.1
Pt/CW-20%-600	8.4	1.79	35.8	19.9

[a] Obtained from CV curves in 0.5 mol L^{-1} H_2SO_4 with a scan rate of 20 mv s^{-1}; $S_{EA} = Q_H / L_{Pt} Q_{Hre}$

which Q_H represents the total charge of hydrogen desorption appearing, L_{Pt} is the mass of platinu the electrode (0.0238 mg), and Q_{Href} is assumed to be 0.21 mC cm^{-2} corresponding to a surface de of 1.3 $\times 10^{15}$ atom cm^{-2} of Pt.

[b] Obtained from CV curves in 2.0 mol L^{-1} CH_3OH + 1.0 mol L^{-1} H_2SO_4 with a scan rate of 20 mv